









Development towards high-resolution kHz-speed rotation-free volumetric imaging

ELENI MYRTO ASIMAKOPOULOU,^{1,15}  VALERIO BELLUCCI,^{2,16}
SARLOTA BIRNSTEINOVA,² ZISHENG YAO,¹  YUHE ZHANG,¹ 
ILIA PETROV,²  CARSTEN DEITER,² ANDREA MAZZOLARI,^{3,4}
MARCO ROMAGNONI,^{3,4} DUSAN KORYTAR,^{5,6} ZDENKO ZAPRAZNY,⁶
ZUZANA KUGLEROVA,⁷ LIBOR JUHA,⁷ BRATISLAV LUKIĆ,^{8,9}
ALEXANDER RACK,⁸  LIUBOV SAMOYLOVA,²
FRANCISCO GARCIA-MORENO,^{10,11}  STEPHEN A. HALL,¹²
TILLMANN NEU,^{10,11} XIAOYU LIANG,¹³ PATRIK VAGOVIC,^{2,14}
AND PABLO VILLANUEVA-PEREZ¹

¹Synchrotron Radiation Research and NanoLund, Lund University, Sweden

²European XFEL GmbH – The European X-Ray Free-Electron Laser, Schenefeld, Germany

³Ferrara University, Department of Physics and Earth Science, Via Saragat 1, 44122 Ferrara, Italy

⁴INFN, Ferrara Division, Via Saragat 1, 44122 Ferrara, Italy

⁵Integra TDS, s.r.o., Krakovany, Slovakia

⁶Institute of Electrical Engineering SAS, Dúbravská cesta 9, 841 04 Bratislava, Slovakia

⁷Department of Radiation and Chemical Physics, Institute of Physics, Czech Academy of Sciences, Prague, Czech Republic

⁸ESRF - The European Synchrotron, Grenoble, France

⁹Henry Royce Institute Department of Materials, The University of Manchester, UK

¹⁰Institut für Werkstoffwissenschaften und -technologien, Technische Universität Berlin, Hardenbergstr. 36 10623 Berlin, Germany

¹¹Helmholtz-Zentrum Berlin für Materialien und Energie GmbH (HZB), Hahn-Meitner-Platz 1, 14109 Berlin, Germany

¹²Division of Solid Mechanics, Lund University, Ole Römers Väg 1, 223 63 Lund, Sweden

¹³Institute of Multidisciplinary Research for Advanced Materials (IMRAM), Tohoku University, 2-1-1 Katahira, Aoba-ku, Sendai, Miyagi 980-8577, Japan

¹⁴Center for Free-Electron Laser Science (CFEL), DESY, Hamburg, Germany

¹⁵eleni_myрто.asimakopoulou@sljus.lu.se

¹⁶valerio.bellucci@xfel.eu

Abstract: X-ray multi-projection imaging (XMPI) has the potential to provide rotation-free 3D movies of optically opaque samples. The absence of rotation enables superior imaging speed and preserves fragile sample dynamics by avoiding the centrifugal forces introduced by conventional rotary tomography. Here, we present our XMPI observations at the ID19 beamline (ESRF, France) of 3D dynamics in melted aluminum with 1000 frames per second and 8 μm resolution per projection using the full dynamical range of our detectors. Since XMPI is a method under development, we also provide different tests for the instrumentation of up to 3000 frames per second. As the high-brilliance of 4th generation light-sources becomes more available, XMPI is a promising technique for current and future X-ray imaging instruments.

© 2024 Optica Publishing Group under the terms of the [Optica Open Access Publishing Agreement](#)

1. Introduction

Time-resolved X-ray imaging has been a fundamental technique for non-destructive exploration of phenomena happening in samples opaque to visible light. The speed and performance of 2D X-ray imaging (radiography) have constantly increased during the last century, with improving

cameras and X-ray sources. State-of-the-art radiography can now record with MHz frame rate speeds at high-brilliance sources such as storage rings [1,2] and X-ray free-electron lasers [3]. On the other hand, time-resolved 3D imaging, also known as tomography, has only recently reached 1 kHz at storage rings [4]. Indeed, the maximum acquisition speed for tomography is limited by the need to rotate the sample, so it induces centrifugal forces that can alter the studied processes. For this reason, it is today still very difficult to capture 3D phenomena in samples opaque to visible light with under-millisecond time resolution. The investigation of many fast phenomena would benefit from this capability, including samples of scientific and industrial interest such as fractures in solids [5,6], shock wave propagation [7,8], fast biological processes [9,10] and fluid dynamic studies [11]. To overcome this problem, there have been developments in the field of X-ray Multi-Projection Imaging (XMPI), which allow for rotation-free 3D imaging [12–16]. XMPI divides the X-ray beam into multiple beamlets to enable imaging of a sample from various angles. The recorded sparse dataset of images is then fed into advanced reconstruction algorithms to obtain a full 3D reconstructed image [17]. Thus, the XMPI method enables the study of dynamics without introducing centrifugal forces that may alter the studied processes [4,18]. In this paper, we demonstrate static and time-resolved XMPI with a frame rate of up to 3 kHz without focusing the beam of ID19 at the European Synchrotron Radiation Facility (ESRF). XMPI was then used for the study of fast stochastic processes in aluminum foam samples. Such samples have been used before for 1 kHz frame-rate tomographic acquisition at synchrotron facilities [4]. Several of the processes of interest that take place in the foam are highly sensitive to the g-forces generated by the fast rotations needed to probe the relevant dynamics, which motivates the use of XMPI for these studies over tomography at higher frame rates. Recently, there have been pioneering attempts to employ XMPI with white beam using different splitting configurations at storage rings [19,20]. Furthermore, a 1.1 MHz sampling method of XMPI was also demonstrated with a two-beamlet configuration [21]. Here we present the first use of XMPI with a full-harmonic beam provided by an insertion device for application in diffraction-limited storage rings. The deployment of XMPI with a narrow energy bandwidth x-ray beam results in images carrying quantitative information on the sample, as well as sharper images, compared to the ones acquired when the technique is used for exploiting a broader spectrum produced by a bending magnet or wiggler that may lead to beam-hardening effect across the different projections [19].

2. Methods

The XMPI method relies on crystal diffraction for the splitting of a primary X-ray beam into secondary beams in order to enable simultaneous imaging of a sample from angularly spaced viewpoints. The configuration of the XMPI setup is adaptable and can be optimized to different facilities, with different beam energies and space availability for the setup. The ID19 ESRF beamline was chosen for this demonstration of XMPI because its undulator source in a diffraction-limited storage ring grants one of the highest spectral densities available for synchrotron sources, 2-3 orders of magnitude higher than beamlines based on bending magnets or wiggler sources [22]. In general, access to a high-brilliance source benefits fast imaging due to the small exposure time for each frame. In the case of XMPI, high-brilliance light sources are crucial, as they enhance the available flux density (photons per second per area), which is a key parameter for our implementation of XMPI. The concepts of the presented implementation of XMPI are introduced in 2.1. The required methods for the optimization of the setup at the conditions of ID19 are motivated and described in 2.2, 2.3 and 2.4.

2.1. XMPI setup

The experimental setup is composed of three main parts; the multi-projection generation, the sample environment, and the detector system. A schematic view of the setup is depicted in Fig. 1. The multi-projection generation is achieved with the use of crystals, which are referred to as

“beam splitters”. Each beam splitter is mounted on motorized stage assemblies with six degrees of freedom (three linear translations and three angles), which allows the alignment of the setup. During alignment, each crystal is positioned in the beam path and oriented at an angle θ with respect to the central beam to fulfill its respective Bragg or Laue condition for a specific part of the spectrum. When the central beam interacts with an aligned beam splitter, part of the beam’s bandwidth is diffracted, creating a secondary beam that travels at a 2θ angle with respect to the central beam and is referred to as a “beamlet”. The portion of the beam that is neither diffracted nor absorbed by a given beam splitter is transmitted. The arrangement of the beam splitters is such that the beamlets intersect at a common point, offering an equal number of projections on the sample. The setup for this work relied on three beam splitters (yet this number will increase in future iterations of the experiment). The exact configuration was finalized after the beam characterization (see Sec. 2.2), as it is further discussed in Sec. 2.3. The sample environment is placed at the beamlet intersection point, allowing its simultaneous imaging from the three generated viewpoints. Because of its design, the XMPI method can accommodate a wide variety of sample environments. The imaging projections are detected with three indirect detectors, each aligned perpendicular to a beamlet’s projection direction. All indirect detectors were identical and were composed of (i) an efficient scintillator ($250\ \mu\text{m}$ thick GAGG+), (ii) a 90° mirror which redirects the visible light to a motorized microscope configuration, (iii) a magnification system consisting of a visible light microscope, which also focuses the light on the camera sensor, and (iv) fast cameras optimized for kHz acquisition speed (Photron Nova S16 models). Each microscope used the same configuration of optics, a 5X Mitutoyo Plan Apo HR Infinity Corrected Objective, and a 1x MT-L tube lens. The described configuration provided a field-of-view of $4 \times 4\ \text{mm}^2$, with an effective pixel size of $4\ \mu\text{m}$. The spatial resolution of the detector system was determined through resolution measurements on vertical and horizontal features of a JIMA RT RC-02B x-ray resolution target. The tracking of the intensity transitions along the horizontal and vertical edge, respectively, was consistent with an error function distribution, that corresponded to the integral of a normalized Gaussian function with full-width at half-maxima (FWHM) of 1.58 pixels and 1.72 pixels respectively. These values are equivalent to $6.30\ \mu\text{m}$ (horizontal) and $6.86\ \mu\text{m}$ (vertical), when taking into account the effective pixel size. In practical terms the spatial resolution of the system is constrained by a Nyquist frequency at two times the effective pixel size, i.e. $2 \times 4\ \mu\text{m} = 8\ \mu\text{m}$.

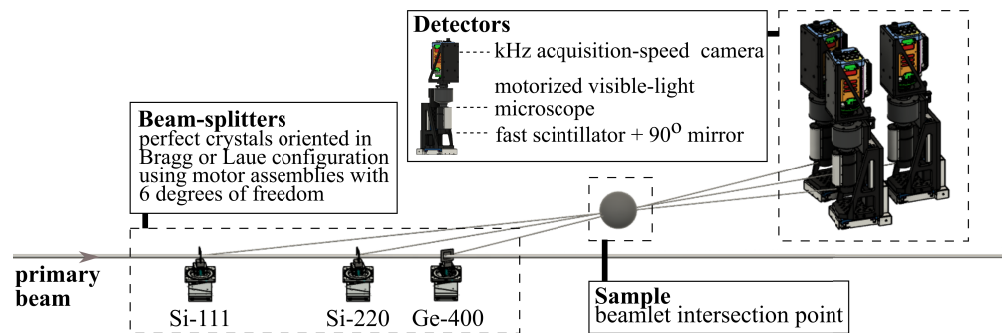


Fig. 1. Illustration of the XMPI concept [16], as implemented at ID-19 of ESRF. The main X-ray beam enters the experimental hall from the left-hand side, propagating to the right of the figure. Three beam splitters are oriented in Bragg or Laue configuration (details in the main text) to meet the Bragg diffraction condition and deflect portions of the main beam’s bandwidth. The beam splitters are positioned so that the deflected beams intersect at one point, where the sample is placed. The detectors are placed behind the sample, each aligned to one of the deflected beams, to image the sample simultaneously from different directions.

2.2. Setup alignment

XMPI is based on crystal diffraction and its configuration is inherently linked to the spectrum and the central energy of the beamline, as it determines the arrangement of the setup. During the experiment we used the U17.6 undulator of the ID19 beamline at the minimum gap of 11.8 mm ($\lambda_u = 17.6$ mm, $N=92$). The on-axis central energy of the beamline (also considered the first harmonic) was expected to be 17.96 keV on-axis with 2% bandwidth (FWHM). These values were obtained from beamline simulations with XOP utilizing parameters of the EBS lattice [23,24]. The off-axis parts of the beam spectrum are filtered out by (i) an insertion aperture, placed 20 m away from the undulator, (ii) a front-end diamond window (0.8 mm thick), placed roughly 27 m from the undulator, with its primary purpose being heat load moderation and vacuum separation, but effectively also dampening energies below 8 keV, (iii) primary power slits, placed 30 m away from the undulator, which cut extensively the outer parts of the central cone and finally (iv) secondary slits, placed 140 m away from the undulator, along with Be and glassy carbon windows, which offer the last filtering. The higher harmonics are not filtered out from the spectrum, since their orders of magnitude lower flux does not make any significant contribution in flux or heat load in this experiment. We implemented a spectrometer to measure the exact beam spectrum and spectrally align the crystals accordingly, i.e. set the crystals in diffraction conditions to the high flux components of the spectrum. The spectrometer was placed as the most downstream element of the setup to act as a monitoring tool [25]. The spectrometer was composed of a bent C-333 crystal, an energy-dispersive element that diffracts different energies with different angles, coupled to a 1x indirect detector PCO.edge.5.5 camera. The diffracted photons are therefore detected in different positions (pixels) in the camera depending on their energy, which allows the monitoring of the beam spectrum. The measurement of the beam's central energy was carried out by first aligning the spectrometer to diffract the most intense part of the beam spectrum and then using a perfect crystal to gauge the angle where its diffraction condition was fulfilled. A perfect silicon crystal with a $\langle 100 \rangle$ out-of-plane direction was used for this purpose and was positioned upstream of the spectrometer. The crystal was rocked continuously in one direction until it was oriented to satisfy the Laue diffraction from the (220) diffraction plane. The central beam spectrum was simultaneously being monitored in the PCO.edge.5.5 camera (Fig. 2). While the silicon crystal was far from satisfying the diffraction condition, the beam spectrum remained unchanged (aside from uniform intensity losses due to transmission through the silicon crystal). When the crystal was rocked in the diffraction region, a clear dip was visible in the camera, indicating the portion of the beam that was being diffracted by the silicon crystal. The dip moved through the beam spectrum as the crystal was rocked through the diffraction region, indicating that the crystal was satisfying the diffraction condition for a different part of the spectrum. The same procedure was repeated with the rocking of the crystal in the opposite direction. The two rocking angles that satisfied the diffraction condition at the most intense part of the spectrum for each of the rocking directions need to be symmetric and were therefore used to assess accurately the diffraction angle for the crystal in the beam's central energy. With this approach, the central energy of ID19 was estimated to be 17.25 keV with the smallest undulator gap, i.e., the highest flux available with 7/8 filling mode and 200 mA storage ring current.

2.3. Beam splitters configuration

The efficiency of the setup is directly affected by the choice of the crystals that act as the beam splitters and the beam parameters (intensity, divergence, spectral components). We positioned different crystals one by one upstream of the calibrated spectrometer in order to characterize their spectral response, i.e., how much of the ID19 beam they diffract. The spectral acceptance of the beam splitters, i.e. the bandwidth percentage that is diffracted as a beamlet, is primarily determined by their respective Darwin width (Table 1). This can be evaluated from the rocking of the beam splitters around their Bragg condition in the primary beam spectrum, as shown in

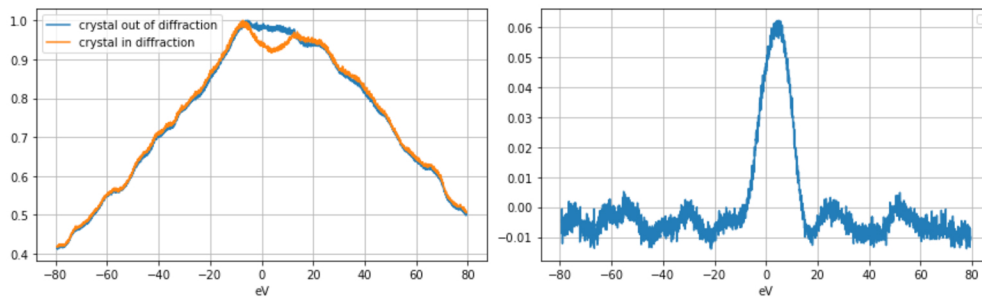


Fig. 2. *Left:* Energy distribution of the 160 eV portion of the primary beam spectrum that interacts with the spectrometer. The blue distribution corresponds to the spectrum measurement when a Si-220 crystal is placed in the beam path, but it is far off the Bragg condition. The orange curve corresponds to the measurement when the Si-220 crystal is oriented to fulfill the Bragg condition for Laue diffraction. *Right:* Distribution of the Si-220 beamlet intensity. The plot has been derived from the two distributions on the left plot. Details on the calibration of the spectrometer can be found in [25].

Fig. 2. Each of the beam splitters is aligned to fulfill the Bragg condition for a part of the energy bandwidth, such that the flux carried by the beamlets is as high as possible. The energy alignment tuning of each beam splitter is therefore unique. If properly aligned this approach allows to repeat this process for more beam splitters. Two limitations are worth mentioning: i) transmission losses, since each beamlet interacts with the portion of the primary beam that has not been diffracted or absorbed by upstream setup elements, and ii) geometry constraints, since the layout is constrained by the need to ensure that the beamlets intersect at a common point. Silicon and Germanium monocrystals were assessed to be optimal for the full-harmonic beam of ID19. The final selection of beam splitters is summarized in Table 1, which will hereafter be referred to using their abbreviations. Simulation of the XMPI setup yield the following expected diffraction efficiency for the crystals: 1.92%, 0.99% and 1.10% for the Si-111, Si-220 and Ge-440 beam splitters respectively. The percentages are estimated for the beam conditions of ID19 and are reported with respect to the primary beam of ID-19, when no other beam splitters interact with the beam. The crystals were provided by INFN-Ferrara. The projection angles of the beam splitters provided 16.28° of angular separation between the beamlet view-points. It is worth noting that the high spectral density of the narrow-bandwidth primary beam allows the beam splitters to tune their acceptance within a similar energy range, thus preserving the quantitiveness of the volumetric information. This is an improvement over other iterations of XMPI, where a polychromatic beams were used, and the beam splitters were tuned to a wider range of energies in order to maximize their diffracted flux, potentially resulting in beam-hardening effects on the sample and affecting the quantitiveness of the recorded images.

2.4. Heat-load measurements

The intensity of the primary beam raises some concerns about the thermal response of the employed beam splitters. The expected thermal response of materials scales with Z^4 , where Z is the atomic number, and their thickness. The final configuration of beam splitters in the experiment included the use of a germanium crystal (see Table 1). Ge-400 crystal was oriented in Bragg geometry and absorbed the entire beam that was not diffracted or absorbed by the previous elements (see Fig. 1). Given the high flux absorbed by this crystal, and its higher atomic number compared to Si, there were concerns about the thermal dissipation of the absorbed heat load within the crystal and we monitored its surface temperature via a thermal camera (FLIR A7600sc). Figure 3 shows the temporal evolution of the temperature registered by the

Table 1. Configuration of the beam splitters for XMPI at beam energy 17.25 keV. The splitters' enumeration (#1-#3) is the order of interaction with the beam. All the beam splitters are mono-crystals. The listed abbreviations are used to refer to the beam splitters in the main text. All values are calculated for the beam conditions of the ID19 beamline. The listed expected diffraction efficiencies of the beam splitters are estimated with respect to the primary beam intensity, when no other beam splitters are present. The position of each element in the setup is determined by the diffraction geometry of the elements. "atb" stands for "along the beam-path", while "ptb" stands for "perpendicular to the beam-path". The positions are mentioned with respect to the position of the first beam splitter.

	Beam splitter #1	Beam splitter #2	Beam splitter #3
Material	Silicon	Silicon	Germanium
Attenuation length	695 μm	695 μm	30 μm
Thickness	14 μm	14 μm	1 mm
Active area	70 \times 50mm ²	5 \times 5mm ²	20 \times 70mm ²
Out-of-plane	<211>	<100>	<100>
Diffraction plane	(111)	(220)	(400)
Diffraction	Laue	Laue	Bragg
Diffraction angle	6.58°	10.79°	14.72°
Projection angle	13.16°	21.58°	29.44°
Darwin width	15 μrad	10 μrad	14 μrad
Expected diffraction efficiency	1.92 %	0.99 %	1.10 %
Abbreviation	Si-111	Si-220	Ge-400
Splitter position (atb, ptb)	(0 mm, 0 mm)	(437 mm, 0 mm)	(626 mm, 0 mm)
Sample position (atb, ptb)	(1069 mm, 250 mm))		

FLIR camera at different exposure times controlled by a shutter (ct) for various time periods. The FLIR camera provides a thermal image as well, which reveals a spatial distribution of temperatures on the irradiated and surrounding surfaces. The temperature rise can be estimated from measured relative intensity ΔC of near-infrared thermal radiation using the proper value of relative emissivity of germanium ε . Emissivity is temperature dependent and thus may vary during the crystal heating. The value of relative emissivity ε for room temperature Ge was measured as $\varepsilon = 0.26$ in [26] and for $T = 1209$ K, i.e. melting point of Ge, as $\varepsilon = 0.55$ in [27]. Since the experiment was performed at room temperature and the change of measured relative intensity was around 2 % of the whole dynamic range, we conclude that the value of relative emissivity coefficient $\varepsilon = 0.26$ reported by [26] for room temperature fits well the conditions of the present experiment. The measured increase in the temperature of the Ge crystal (Fig. 3) is of the order of tens of degrees and well below the melting point of Ge. No distortion is visible in the images from the Ge-400 projection. This includes distortions due to thermal strain caused by overheating the crystal. Therefore, we can conclude that the heat transfer from the crystal surface to the crystal bulk, the air, and the crystal holder is effective enough to prevent the overheating of the irradiated region. The heat dissipation measurements on Ge-400 also served as a safety margin for any concerns on the heat dissipation in Si. Si has a lower atomic number and a higher melting point (1683 K), while the thickness of the Si-111 and Si-220 beam splitters was much smaller than that of Ge-400. Furthermore, we did not observe image distortions over long exposure times on the Si-220 splitter. We assessed that there should not be any concerns on thermal loading effects for the Si beam splitters.

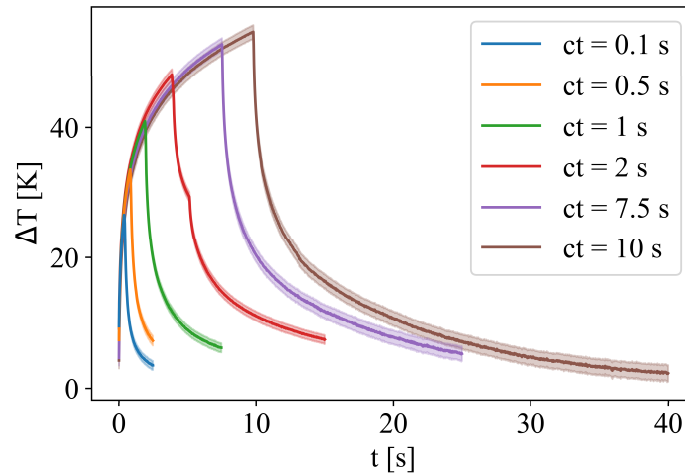


Fig. 3. Measured temperature change ΔT versus time t on the last crystal Ge-400 for different times of opened shutter ct . The error bar is visualized as a shade. The temperature change is far from the melting point of germanium $T = 1209$ K.

3. Results and discussion

An alignment sample (bamboo toothpick) was used to determine and monitor the intersection of the Si-111, Si-220, and Ge-400 beamlets. The final configuration allowed recording up to 3 kHz with the three cameras simultaneously using the whole 12-bit dynamical range of the kHz cameras. This corresponds to frame acquisitions every 0.3 ms, allowing the reconstruction of sub-millisecond dynamics. Each new recording could be sustained for 7.273 s. The microscope configuration has $8 \mu\text{m}$ spatial resolution per frame, estimated using a resolution target. The recorded images with all three cameras can be seen in Fig. 4. The Si-111 image in Fig. 4 was rotated by 5.81° to recover a misalignment error in the camera.

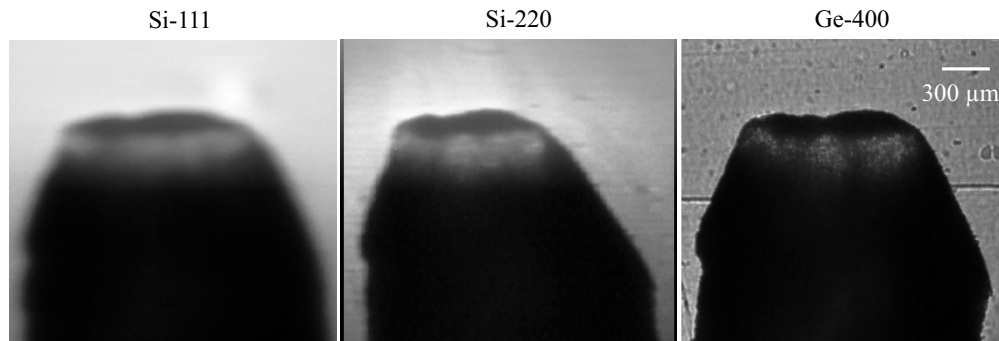


Fig. 4. Simultaneous frame acquisition of an alignment pin at 3000 fps speed from three projections, coming respectively from the beam splitters Si-111, Si-220, Ge-400. The Si-111 and Si-220 beam splitters are in Laue geometry, while the Ge-400 is in Bragg. The blurring in the Si-111 and Si-220 projections is caused by the crystal effects combined with some warping in these thin membrane-like splitters.

The illumination of the alignment sample allowed some observations about the employed beam splitters. The Ge-400 projection appears intense and clear and is used as a reference for the capabilities of the setup. However, the Si-111 and Si-220 projection images appear blurry

(Fig. 4). After dedicated testing, it was concluded that the cause of the blur in the Si-111 and Si-220 images was the result of two factors: crystal effects and the presence of strain in the crystals. We attribute part of the blurring in the Si-111 and Si-220 images to crystal effects because we observe different resolutions in the plane of diffraction, compared to the perpendicular plane. One crystal effect that is believed to contribute to the blurriness is the Borrmann triangle [28], which is a dynamical diffraction effect. Indeed, an X-ray beam diffracted over the entire thickness of a crystal results in a distribution of the diffraction centers over a fan-shaped profile, which produces a blurry virtual source. An additional crystal effect believed to contribute to the blurriness is the resolution limit of the Si-111 and Si-220 crystals, which are determined by the crystals' diffraction planes [29]. Finally, Laue diffraction is especially sensitive to strain in the crystal since strained areas are illuminated differently, for example under the profile of the fanned diffracted beam. An example of this can be seen at the top of the Si-220 projection image, where a halo appears. The measurements were carried out with a low-strain area of the crystal to mitigate these effects. We do not observe the same blurring in the Ge-400 images. Further quantitative analysis is needed to evaluate the effects that introduce the blurriness and their level of contribution. It is also important to perform pre-characterization of the crystals for this analysis, including an accurate measurement of the crystals' thickness, as this significantly changes the Borrmann effects.

In the Si-220 projection, the significant strain produces a curvature in the crystal shape that results in warping of the beam trajectories, stretching the recorded projections along this beam. Because of this stretching and the aforementioned crystal effects, the Si-220 figure was re-scaled over the horizontal direction by a factor of 1.17 to match the real aspect ratio of the object. The scaling factor was derived by assuming that the metallic-foam bubbles are spherical and need to match in size in the images recorded from the Ge-400 and Si-220 beamlets along the diffraction plane. It was also verified that this ratio was valid for the Si-220 diffraction plane direction when comparing to the perpendicular one. The strain was most likely introduced during fabrication or by the clamping method. Both causes are technological in nature and they can be improved upon with further engineering of the crystals and their holders. Regarding the Si-111 splitter, we observe strong vibrations. The Si-111 beam splitter is indeed susceptible to vibrations due to the fact that it is a very thin, free-standing crystal (i.e. there is no frame around the active area) with a large active area. In future iterations, we will redesign the mounting and rethink the design of the crystal.

To demonstrate the capabilities of XMPI at ID19, we explore the foaming of an aluminum alloy produced by a fast and self-triggering pressure release method. The complete foaming and solidification process of the alloy takes place in less than one second and has never been studied before at such speeds. Rapid metal foaming and solidification not only have the advantage of short production time but also of rapid development, as the foam structure has much less time to coarsen. Time is one of the most important parameters, along with temperature and alloy composition, leading to an increased number of coalescence events [30]. Long foaming times lead to an increased number of coalescence events and, thus, to foam aging.

This process demonstrated dynamics at the order of 0.5-1 kHz, so we optimized our acquisition system to that range. Although similar samples have been observed in 3D at kHz frame rate during a standard metal foaming process, it was also observed that in some cases, the dynamics of low-stabilized liquid metal foams such as the alloy studied in this work were altered in the later foaming stage by the radial forces generated by the rotation [4]. Thus, XMPI is a promising technique for their study without sample rotation and, therefore, without altering the dynamics of interest. The studied sample was produced from a foamable thixocast precursor made of an AlSi6Cu4 alloy with an added 0.8 wt% TiH₂ as a blowing agent. Thixocast foamable precursors are known for their high volume expansion and capability to form round bubbles but also for their tendency for bubble coalescence [31]. By observing the evolution of such liquid metal foams in

3D, we gain insight into fast phenomena during the foaming process, such as the evolution of film thickness, i.e. the distance between bubbles, over time, the minimum film thickness, gas interdiffusion between different bubbles, or the rupture and coalescence of bubbles orders of magnitude faster than normal foam expansion.

The measurements were carried out with two out of the three beam splitters (Si-220 and Ge-400) of the final XMPI configuration since the illumination from the Si-111 beam splitter was experiencing intense drifting, making the recording unusable. The remaining view-points had an angular separation of 7.86° . During the measurements, the expansion of the foams occurs rapidly due to the fast intrinsic pressure release, making it non-trivial to determine the correct time to trigger the acquisition. The detector initially assigned for the Si-111 crystal was repurposed to provide a visual trigger to begin the acquisition process. A laser was set to illuminate the sample so that the visible light image captured on the camera had the same field-of-view as the X-ray images provided by the other two cameras, i.e. it was a close representation of the expected X-ray images. Therefore, the view from this camera was used to manually trigger the acquisition of the two other cameras when the expanding foaming was visible in the field of view.

The 3D structure of metallic foams was reconstructed using a deep learning 3D reconstruction approach. We applied ONIX [17], a self-supervised learning method developed to address the ill-defined problem posed by XMPI. A continuous function [32,33] was trained that maps from the spatial-temporal coordinates to the refractive index of the sample, depicting the structure of the metallic foams. Given the limited volumetric data available from the two projections, we adopted adversarial learning [34] to enforce the self-consistency between the collected projections and the predictions generated from arbitrary viewpoints. An additional discriminator as the one used in [35] was added to the ONIX architecture, and the networks were trained using the adversarial loss function [34,36]. We selected a region of interest with the size of 128×128 on both projections for the 3D reconstruction, as shown in Fig. 5. The selected areas were denoised using total variation filters and segmented from the background before feeding into the neural networks. The network training was performed on an NVIDIA A100 GPU with 40 GB of RAM. We used Adam optimizer [37] with a learning rate of 10^{-4} and batch size of eight. After the training, the volumetric information was obtained by extracting 128^3 grids from the networks, with the voxel size equivalent to the effective pixel size of $4 \mu\text{m}$. The resulting 3D reconstructions were visualized using Blender. A selection of frames from the two projections can be seen in Fig. 5. In the shown projections, slight bubble movements are visible and the rupture of a surface bubble can be observed, which results in a dark corrugated structure at its former position and will be discussed later in more detail. More accurate results are visible in the reconstructed 3D volume. It should be noted that ONIX operates as a data-driven approach. Its performance is therefore highly dependent on the quality and quantity of the training dataset. Increasing the number of experiments on similar samples would thus enhance greatly the performance of the model for the reconstruction, even in such experiments with two projections.

When the distance between two adjacent bubbles, in this case of relatively equal size, falls below a certain critical level, the film rupture leads to the coalescence of the bubbles, resulting in a new round bubble in a time frame of 1-2 ms, as shown in Fig. 6. The volume of this new bubble is nearly equal to the sum of the volumes of the previous bubbles, neglecting a slight expansion due to a reduced Laplace pressure. As the bubbles involved are relatively small compared to others and to the foam size, no significant bubbles or foam rearrangements are observed in the surrounding area in this case. Similar behavior has been observed in the past with other alloys with X-ray radioscopy [38]. The kinetics of coalescence are random in nature but influenced by various parameters such as gravity or temperature [39]. To gain a more detailed insight into this coalescence process, even faster acquisition speeds will be required. This conclusion is consistent with the X-ray tomography results for a more stable liquid metal foam alloy [40].

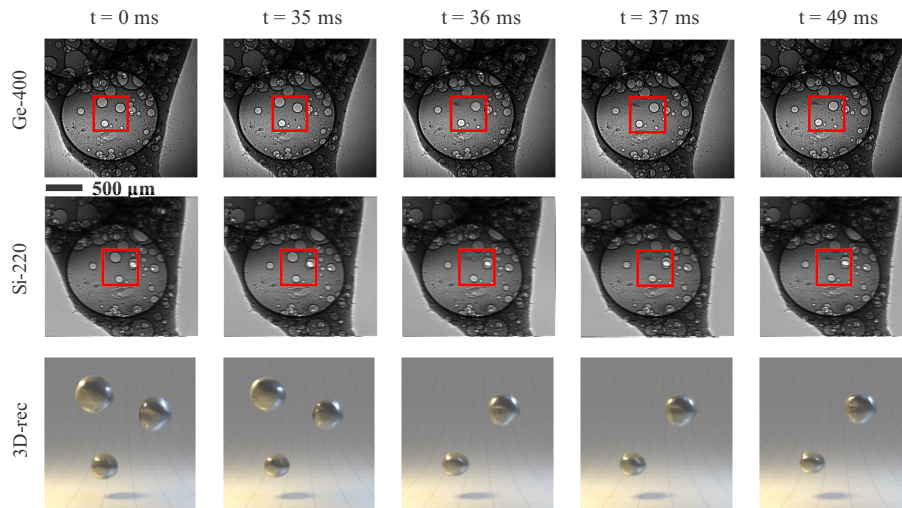


Fig. 5. A selection of frames was collected with two projections of the XMPI method during the foaming of an AlSi6Cu4 thixocast precursor. The red square marks the region of interest for the reconstruction, while the first ($T=0.000s$) and last ($T=0.049s$) timestamps mark the time period that was used for the reconstruction. In the interim consecutive frames ($T=0.035s$, $T=0.036s$ and $T=0.037s$), behaviors in the bubble movement can be monitored. The last row shows renderings of 3D reconstructions of the selected bubbles. At $t = 36$ ms, the upper left bubble burst with no significant effect on the rest of the bubbles' position, volume, or rearrangements in the neighborhood. 3D videos are available in [Visualization 1](#).

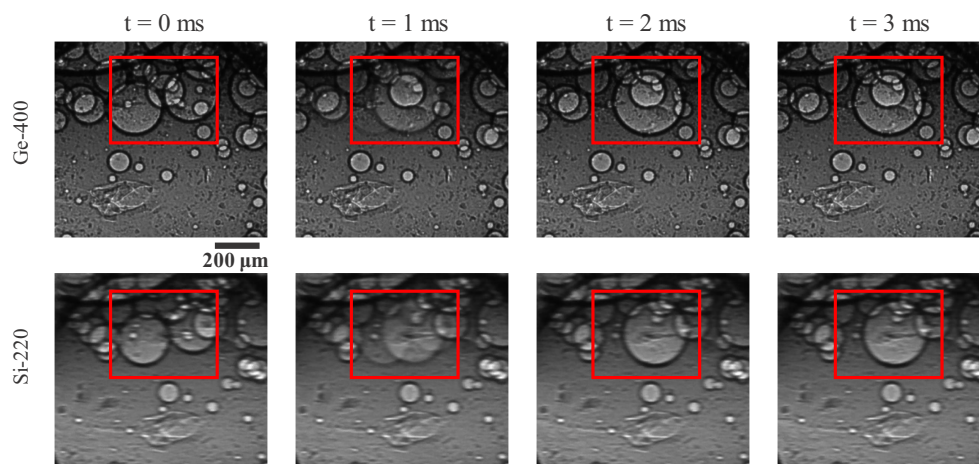


Fig. 6. Bubbles merging in the melted aluminum foam sample. The selection of frames shows two similarly sized bubbles merging into one larger one, details marked by the red square. This process takes a maximum of 1-2 frames, i.e. of 1-2 ms. Videos of the radiosopic sequence are available in [Visualization 2](#).

If the bubbles involved in a coalescence process are large relative to the foam size, as shown in Fig. 7, the film rupture process leading to coalescence of the bubbles can be accompanied by a coalescence avalanche [41] and a vigorous structural rearrangement of the entire foam, which directly affects the development of foam expansion. The film rupture is again faster than 1 ms and the coalescence of the two bubbles takes place in a few milliseconds.

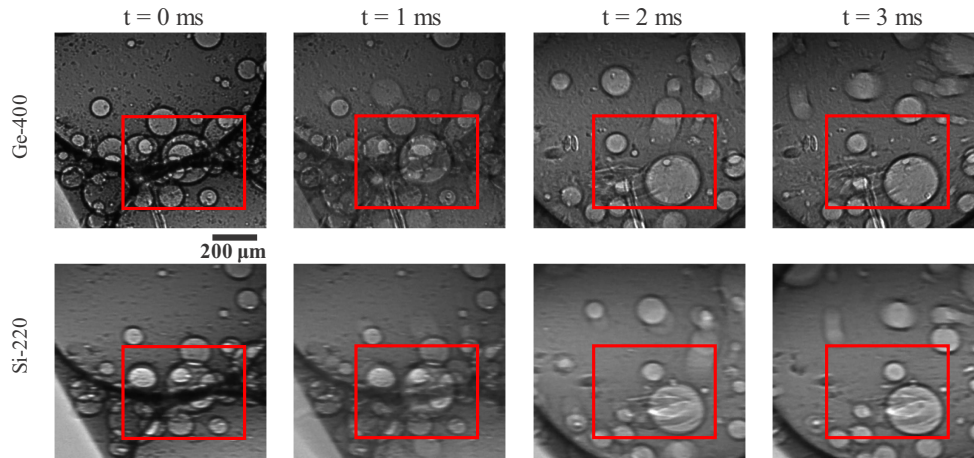


Fig. 7. Selection of frames showing bubble coalescence and rupture in the melted aluminum foam sample. The red square marks the region of interest where a film between two relatively large bubbles ruptures, leading to coalescence of the two bubbles involved, and also to an avalanche of further bubble coalescence and structural rearrangements. Videos of the radiosopic sequence are available in [Visualization 2](#).

A new phenomenon, namely the formation of spikes on the foam surface, was observed and is shown in a sequence in Fig. 8. When a bubble bursts near the surface, a film rupture occurs at the outer foam skin, with molten material spurting out in less than a millisecond. The spike-like surface protrusions form in 1-2 ms. They can be stabilized either by the solid oxide skin on the surface or by a small solidified liquid portion, as they are not immediately retracted by the surface tension of the liquid. This point has to be studied in more detail in the future. The formation of such spikes could only be observed in cases where foam growth and subsequent foam solidification are extremely rapid, as is the case here.

This experiment has underlined the potential of the technique for imaging sample dynamics that are sensitive to centrifugal forces and also set the opportunity to discuss its limitations. The technique generates secondary beams (beamlets) for the illumination of the sample through Bragg diffraction. The intensity of the diffracted beam is inherently linked with the acceptance of the crystals. Each beam-splitter is able to diffract roughly two orders of magnitude of the full harmonic, thus introducing a limitation to the intensity of illumination on the sample. The technique also offers sparse volumetric information when compared with other 3D imaging techniques, such as tomography. To overcome this limitation, we combine XMPI with dedicated deep-learning 3D algorithms for the reconstruction of the volumetric information. The performance of the deep learning algorithms is dependent on the quantity of the training datasets. By collecting multiple experiments of similar samples, even with two projections, the performance of the model is enhanced. The diversity of the training dataset can be expanded by randomly orienting or manually shifting samples at various angles. This way, the neural networks receive more information about the sample, contributing to improved model performance. Finally, the technique relies on an complex setup, as it requires a large number of technical equipment with geometric constraints on their placement, as determined by the Bragg diffraction conditions of the beam splitter.

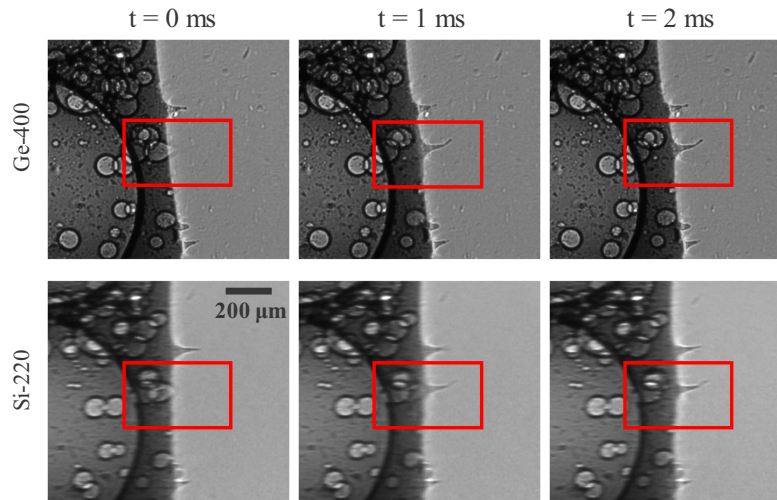


Fig. 8. A selection of magnified frames showing the rupture of a film at the foam surface leading to the burst of a bubble and the generation of a surface spike in the course of fast solidification. Videos of the radiosopic sequence are available in [Visualization 2](#).

4. Conclusions

This experiment constitutes the first implementation of XMPI at a diffraction-limited storage ring using the full-harmonic beam provided by an insertion device. The XMPI technique, coupled with the high spectral density and full-harmonic beam of the ID19 beamline, allowed to successfully image sub-millisecond dynamics (3000 frames per second) with spatial resolution of $8\ \mu\text{m}$ per projection while filling the full dynamic range of the detectors. The narrow energy bandwidth of this implementation enables the images to carry quantitative information on the sample, as well as produce sharper images compared to a white beam. In polychromatic beams the XMPI beam splitters select a very broad energy bandwidth which can potentially result in beam-hardening effects on the sample and affect the quantitiveness of the recorded images. Thus, the results presented here are a fundamental step to establish XMPI as a technique capable of probing 4D (3D+time) phenomena in samples opaque to visible light with kHz frame-rate speed and micrometer resolution that are sensitive to centrifugal forces.

XMPI was employed for the study of the dynamics of the aluminum foaming process at 1 kHz, avoiding centrifugal forces that alter the studied dynamics as introduced by time-resolved tomography in such systems. From the acquired dataset, 3D movies of bubbles moving in the melted aluminum were obtained via machine learning algorithms. The absence of centrifugal forces was crucial to enable the observation of a novel phenomenon in aluminum foaming, namely the formation of spikes on the foam surface. These spikes are formed by the bursting of small bubbles near the sample surface and solidify quickly due to the colder ambient temperature and the formation of an oxide layer. Furthermore, the rupture of small and large films separating two bubbles and leading to their coalescence could be investigated for the first time at 1 kHz in a liquid AlSi6Cu4 alloy foam. In agreement with other results in the literature, film rupture times of less than 1 ms could be detected, indicating the need for even faster acquisition speed.

As a result of this implementation, we are designing a beam-splitting scheme tailored to the beam characteristics of ID19 that will allow additional projections with increased angular spacing between each projection to benefit the 3D reconstruction process. Furthermore, this future implementation of the XMPI instrument will increase the spatiotemporal resolution by enhancing

the efficiency and image quality of the crystal splitters by using symmetric Bragg diffraction and improving the crystal mounting and crystal fabrication (thickness, polishing quality and flatness).

Funding. Röntgen-Ångström Cluster (“INVISION” project 05K18KTA, 2019-2023); EuXFEL R&D (2020 - 2022, MHz microscopy at EuXFEL); HORIZON EUROPE European Research Council (ERC-2020-STG, 3DX-FLASH, Grant agreement 948426); HORIZON EUROPE European Innovation Council (Pathfinder “MHz-Tomoscopy” project, 2022-2025); Ministerstvo Školství, Mládeže a Tělovýchovy (LM2023068); Slovenská Akadémia Vied (VEGA - 2/0041/21).

Acknowledgments. We thank the team of ESRF ID19 for the help during beamtime MI1449. We also wish to acknowledge Julia Katharina Rogalinski for her work on the calculations of the spatial resolution of the detector systems that were used in this work.

Disclosures. The authors declare no conflicts of interest.

Data availability. Data underlying the results presented in this paper are not publicly available at this time but may be obtained from the authors upon reasonable request.

References

1. K. Fezzaa and Y. Wang, “Ultrafast x-ray phase-contrast imaging of the initial coalescence phase of two water droplets,” *Phys. Rev. Lett.* **100**(10), 104501 (2008).
2. M. P. Olbinado, X. Just, J.-L. Gelet, *et al.*, “Mhz frame rate hard x-ray phase-contrast imaging using synchrotron radiation,” *Opt. Express* **25**(12), 13857–13871 (2017).
3. P. Vagovič, T. Sato, L. Mikeš, *et al.*, “Megahertz x-ray microscopy at x-ray free-electron laser and synchrotron sources,” *Optica* **6**(9), 1106–1109 (2019).
4. F. García-Moreno, P. H. Kamm, T. R. Neu, *et al.*, “Tomoscopy: Time-resolved tomography for dynamic processes in materials,” *Adv. Mater.* **33**(45), 2104659 (2021).
5. A. Kumar, K. Kashyap, M. T. Hou, *et al.*, “Strength improvement of glass substrates by using surface nanostructures,” *Nanoscale Res. Lett.* **11**(1), 256 (2016).
6. Z. Xu, X. He, Y. Han, *et al.*, “A different viewpoint on mechanism of fracture to shear-banding failure mode transition,” *J. Mech. Phys. Solids* **145**, 104165 (2020).
7. Y. B. S. R. Prasad, S. P. Barnwal, P. A. Naik, *et al.*, “Shock wave propagation in soda lime glass using optical shadowgraphy,” *Pramana* **87**(1), 9 (2016).
8. D. E. Grady, “Shock-wave compression of brittle solids,” *Mech. Mater.* **29**(3-4), 181–203 (1998).
9. J. N. Hansen, A. Gong, D. Wachten, *et al.*, “Multifocal imaging for precise, label-free tracking of fast biological processes in 3D,” *Nat. Commun.* **12**(1), 4574 (2021).
10. T. V. Truong, D. B. Holland, S. Madaan, *et al.*, “High-contrast, synchronous volumetric imaging with selective volume illumination microscopy,” *Commun. Biol.* **3**(1), 74 (2020).
11. A. Aliseda and T. J. Heindel, “X-ray flow visualization in multiphase flows,” *Annu. Rev. Fluid Mech.* **53**(1), 543–567 (2021).
12. P. Villanueva-Perez, B. Pedrini, R. Mokso, *et al.*, “Hard x-ray multi-projection imaging for single-shot approaches,” *Optica* **5**(12), 1521–1524 (2018).
13. J. Duarte, R. Cassin, J. Huijts, *et al.*, “Computed stereo lensless X-ray imaging,” *Nat. Photonics* **13**(7), 449–453 (2019).
14. W. Voegeli, K. Kajiwar, H. Kudo, *et al.*, “Multibeam x-ray optical system for high-speed tomography,” *Optica* **7**(5), 514–517 (2020).
15. V. Bellucci, M. Zdora, L. Mikeš, *et al.*, “Hard x-ray stereographic microscopy for single-shot differential phase imaging,” *Opt. Express* **31**(11), 18399–18406 (2023).
16. P. Vagovic, V. Bellucci, P. Villanueva-Perez, *et al.*, “Multi beam splitting and redirecting apparatus for a tomoscopic inspection apparatus, tomoscopic inspection apparatus and method for creating a three dimensional tomoscopic image of a sample,” (Patent pending, Application number: EP21200564.9).
17. Y. Zhang, Z. Yao, T. Ritschel, *et al.*, “Onix: An x-ray deep-learning tool for 3d reconstructions from sparse views,” *Appl. Res.* **2**(4), e202300016 (2023).
18. B. Jachimska and K. Malysa, “Foam rupture under combined action of gravity and centrifugal force,” *Bull. Pol. Acad. Sci. Chem.* **48**, 166–179 (2000).
19. X. Liang, W. Voegeli, H. Kudo, *et al.*, “Sub-millisecond 4d x-ray tomography achieved with a multibeam x-ray imaging system,” *Appl. Phys. Express* **16**(7), 072001 (2023).
20. W. Voegeli, X. Liang, T. Shirasawa, *et al.*, “Multi-beam x-ray optical system for high-speed tomography using a σ -polarization diffraction geometry,” *Appl. Phys. Express* **16**(7), 072007 (2023).
21. P. Villanueva-Perez, V. Bellucci, Y. Zhang, *et al.*, “Megahertz x-ray multi-projection imaging,” *arXiv*, arXiv:2305.11920 (2023).
22. T. Weitkamp, P. Tafforeau, E. Boller, *et al.*, “Status and evolution of the ESRF beamline ID19,” *AIP Conf. Proc.* **1221**, 33–38 (2010).
23. M. S. del Río and R. J. Dejus, “XOP v2.4: recent developments of the x-ray optics software toolkit,” *Proc. SPIE* **8141**, 814115 (2011).

24. P. Raimondi, C. Benabderrahmane, P. Berkvens, *et al.*, “The extremely brilliant source storage ring of the european synchrotron radiation facility,” *Commun. Phys.* **6**(1), 82 (2023).
25. V. M. Kaganer, I. Petrov, and L. Samoylova, “Resolution of a bent-crystal spectrometer for X-ray free-electron laser pulses: diamond versus silicon,” *Acta Crystallogr. Sect. A* **77**(Pt 4), 268–276 (2021).
26. H. Madura, H. Polakowski, and B. Wiecek, “Spectral emissivity evaluated for materials used in microelectronics,” *Quantitative Infrared Thermography QIRT 96 – Eurotherm Series* pp. 52–57 (1997).
27. F. G. Allen, “Emissivity at 0.65 Micron of Silicon and Germanium at High Temperatures,” *J. Appl. Phys.* **28**(12), 1510–1511 (1957).
28. A. Authier, *Dynamical Theory of X-Ray Diffraction* (International Union of Crystallography, 2001).
29. R. Spiecker, P. Pfeiffer, A. Biswal, *et al.*, “Dose-efficient in vivo x-ray phase contrast imaging at micrometer resolution by bragg magnifiers,” *Optica* **10**(12), 1633–1640 (2023).
30. F. García-Moreno, M. Jürgens, and J. Banhart, “Temperature dependence of film rupture and internal structural stability in liquid aluminium alloy foams,” *Acta Mater.* **196**, 325–337 (2020).
31. J. Weise, H. Stanzick, and J. Banhart, “Semi-solid processing of complex-shaped foamable material,” (2003).
32. B. Mildenhall, P. P. Srinivasan, M. Tancik, *et al.*, “NeRF: Representing Scenes as Neural Radiance Fields for View Synthesis,” in *Lecture Notes in Computer Science (including subseries Lecture Notes in Artificial Intelligence and Lecture Notes in Bioinformatics)*, vol. 12346 LNCS (Springer Science and Business Media Deutschland GmbH, 2020), pp. 405–421.
33. A. Yu, V. Ye, M. Tancik, *et al.*, “pixelnerf: Neural radiance fields from one or few images,” in *Proceedings of the IEEE/CVF Conference on Computer Vision and Pattern Recognition*, (2021), pp. 4578–4587.
34. I. Goodfellow, J. Pouget-Abadie, M. Mirza, *et al.*, “Generative adversarial networks,” *Commun. ACM* **63**(11), 139–144 (2020).
35. C. Ledig, L. Theis, F. Huszár, *et al.*, “Photo-realistic single image super-resolution using a generative adversarial network,” in *Proc. Computer Vision and Pattern Recognition*, (2017), pp. 4681–4690.
36. K. Schwarz, Y. Liao, M. Niemeyer, *et al.*, “Graf: Generative radiance fields for 3d-aware image synthesis,” *Adv. Neural Inf. Process. Syst.* **33**, 20154–20166 (2020).
37. D. P. Kingma and J. Ba, “Adam: A method for stochastic optimization,” *arXiv*, arXiv:1412.6980 (2014).
38. F. Garcia-Moreno, M. Mukherjee, C. Jiménez, *et al.*, “Metal foaming investigated by x-ray radioscscopy,” *Metals* **2**(1), 10–21 (2011).
39. F. Garcia-Moreno, E. Solórzano, and J. Banhart, “Kinetics of coalescence in liquid aluminium foams,” *Soft Matter* **7**(19), 9216–9223 (2011).
40. F. García-Moreno, P. H. Kamm, T. R. Neu, *et al.*, “Using x-ray tomoscopy to explore the dynamics of foaming metal,” *Nat. Commun.* **10**(1), 3762 (2019).
41. M. Paeplow, F. García-Moreno, A. J. Meagher, *et al.*, “Coalescence avalanches in liquid aluminum foams,” *Metals* **7**(8), 298 (2017).